Die-Level Micrometers-Deep Subsurface Imaging for Fault Isolation Using Remote Bias Induced Electrostatic Force Microscopy

Evgheni Strelcov*[1]*, Lin You*[2]*, Yaw Obeng, and Joseph J. Kopanski

Nanoscale Device Characterization Division, National Institute of Standards and Technology,
Gaithersburg, Maryland 20899-8120, United States
Electronic mail: evgheni.strelcov@nist.gov, joseph.kopanski@nist.gov

[1]Institute for Soft Matter Synthesis and Metrology, Georgetown University, Washington, DC 20057, United States
[2]Current Address: Micron Technology Inc., Boise, ID, 83707, United States

Abstract

In recent years, scanning probe microscopy (SPM) has drawn substantial attention for subsurface imaging, since the ultra-sharp AFM tip (≈ 10 nm in radius) can deliver and detect, mechanical and electrical signals right above the material's 3D volume with which it is directly interacting. Electrostatic force microscopy, or EFM, is one of the most common atomic force microscopy (AFM) variants for electrical property characterization. In this work, we demonstrate a method to significantly improve EFM's subsurface imaging capability. Unlike conventional EFM, where an AC bias is applied to the cantilever, we applied two out of phase AC biases to adjacent subsurface lines and image the resulting cantilever response at the surface. The resulting remote bias induced EFM (RB-EFM) amplitude shows decent contrast of metal lines with a 2.4 µm spacing buried up to 4 µm beneath the surface. This novel method may resolve lines with a horizontal spacing of less than 130 nm at such depth and wider lines to at least 6 µm in depth. In addition, the results are compared with conventional EFM and KPFM that detects subsurface structure with two independent DC biases. A COMSOL simulation model has been developed that reproduces the essential features of the measurement and explains the improvement of subsurface imaging with RB-EFM compared to other electrostatic force imaging techniques. We show, that by biasing independent lines at a small delta in frequency from the cantilever resonance, multiple line traces can be differentiated in the RB-EFM image.

Introduction

The fast-growing nanotechnology and nanobiology (i.e. cytology) fields demand advanced characterization methods, not only for structural and functional properties of materials' surfaces, but also into their 3D volume. In the past few decades, optical microscopy, electron microscopy (EM) [1-6] and atomic force microscopy (AFM) [7-12] have been the main approaches to resolve materials behavior on the sub-micrometer scale. Optical microscopy and spectroscopy have large penetration depth for optically transparent samples and allow for chemical characterization. However, its lateral resolution is limited by light diffraction to ca. 200 nm (although, fluorescence microscopy can resolve features down to 10 nm). Light scattering in dispersive or non-transparent media also limits light microscopy. EM methods have a high lateral resolution (down to atomic level) and are sensitive to crystalline structure and elemental composition. In the EM approach to subsurface imaging, variable accelerating voltages [3, 13-16] are typically used to penetrate the sample which results in electron-matter interactions, including secondary electron generation, as well as plasmon excitations and/or Rutherford scattering, especially in thick samples [2]. EM's applicability is limited to high or low vacuum, or imaging through membranes [17]. The vacuum is needed to allow the electrons to travel within the instrument unimpeded, and to prevent cathode oxidation and electrical discharge in the gun assembly.

The increasing complexity of integrated circuits (IC's) and the need for advanced packaging technologies necessitates the development of failure analysis tools capable of non-destructive subsurface imaging of interconnects and their electric potentials. Due to the opaque nature of packaging and lack of light probe sensitivity to electric fields, optical microscopy has limited applicability. X-ray methods, having excellent penetration capabilities, are also insensitive to bias. Electro-magnetic and thermal fields can penetrate through the insulating and packaging materials, making electrical fault detection possible with magnetic and thermal imaging. The later employs SQUID or giant magnetoresistance (GMR) sensors [18-20]. Magnetic field maps, generated by the flowing currents were recorded and then converted into current maps by inverse problem solving to image shorts, leakage and high resistance points in IC's. Open failures in IC's were detected by sending a radio-frequency wave into the open trace and creating a standing wave reflected off the open end of the line. The standing wave was then imaged with a magnetic sensor. While the SQUID and GMR sensors showed an impressive lateral resolution of a few micrometers and 250 nm, respectively, at an imaging distance of 700 micrometers [18], this method is not readily available for use and remains a complex and expensive technique.

Compared with the above-mentioned techniques, AFM is simpler, widely available, and can be used in various fluid environments [21] as well as in a vacuum, to image non-conductive samples [22] and detect thermal, magnetic, and electric fields. AFM resolution is not limited by diffraction, only by the size of the probe-sample interaction volume (i.e., point spread function), and can be as high as atomic [23]. Here we focus on subsurface imaging using AFM electric field-sensitive techniques: scanning impedance microscopy (SIM) [24-25], electrostatic force microscopy (EFM) [26-30], and Kelvin probe force microscopy (KPFM) [31] in both amplitude modulation (AM) and frequency modulation (FM) modes. All these techniques are non-invasive and rely on the long-range electrostatic interaction between the sample (or subsurface metal electrode) and AFM tip positioned some distance above the sample's surface. The electrostatic force acting on the AFM tip in the vertical direction is given by:

$$F_z^{el} = \frac{1}{2} C_z' \Delta V^2 \tag{1}$$

where C'_z is the first derivative of capacitance along the vertical direction, z, and ΔV is the potential difference between the tip and sample. To enhance sensitivity, detection of this force is performed away from the DC limit at one of the resonance frequencies of the AFM cantilever. For that, an AC voltage bias (V_{AC}) at that frequency is applied to the conductive AFM tip (for EFM and KPFM) or the sample (SIM), while a DC bias (V_{DC}) can be applied to the tip (SIM) or sample (EFM, KPFM). The AFM cantilever is mechanically excited at another resonance frequency, and the amplitude and frequency of its oscillation are affected by the electric force, allowing the detection of the later via lock-in amplitude and phase (AM mode) or frequency shift (FM mode). The first harmonic of the electric force in the vertical direction under the influence of an AC voltage $V(t) = V_{AC}\cos(\omega t)$ and a DC voltage V_{DC} is given by:

$$F_{z1\omega}^{el} = C_z' \Delta V_{ts} V_{AC} \tag{2}$$

Here ΔV_{ts} is the local DC voltage difference between the tip and sample, which includes the contact potential difference:

$$CPD = \frac{\Phi_{tip} - \Phi_{sample}}{e} - V_{sample}, \tag{3}$$

where Φ is the material's work function and e is the elementary charge). KPFM allows the measurement of CPD by applying a DC voltage to the tip until the force (and ΔV_{ts}) vanishes, making the applied DC voltage equal to CPD. Subsurface imaging of carbon nanotubes in a polymer matrix was first demonstrated using SIM in 2004 with a probing depth of ca. 100 nm [32]; and later by EFM [11, 33-35]. In this report we demonstrate the usefulness of a modified SIM method, or remote bias induced EFM (RB-EFM), for imaging metal lines buried several micrometers deep in an insulator, as is used in integrated circuit interconnects and advanced packaging. An increase in probing depth and resolution is achieved via the application of an AC bias to adjacent metal lines with a 180° phase shift between them. Thus, the force exerted on the tip by one line will be proportional to (V_{DC} + ½ V_{AC}) and by the other to (V_{DC} - ½V_{AC}), improving the contrast. Phase difference, the AC and DC voltage amplitude dependences of the signal, as well as comparison with EFM and KPFM data, are presented. We show that discrimination between different electrodes can be made based on the frequency of the AC bias or its amplitude. The collected experimental data are confirmed by numerical modeling using COMSOL Multiphysics[1]. The probing depth and resolution of the RB-EFM depends on the experimental parameters and is determined by the electric field strength.

Dedicated test chips used in this work were manufactured with the Taiwan Semiconductor Manufacturing Company 0.35-µm technology process flow, with four different levels of metallization [36]. While we do not know all the proprietary processing details used in the fabrication of these devices, it is reasonable to assume that the metal lines consist of a Ti (barrier)/Al−1.0 %Si−0.5 %Cu/TiN (cap). CF_4 plasma or O_2 plasma post-etch treatment was probably performed after metal etch to passivate the Al lines. Sintering was done at 400°C for 10 min. in forming gas (2 % H_2/98 % Ar) at the end of the process flow. The inter-level dielectric consists of a plasma-enhanced chemical vapor deposited-tetraethylorthosilicate (PECVD-TEOS) SiO_2 layer. The dielectric films were planarized by chemical-mechanical polishing. It appears an etch-back process was used to remove excess dielectric in the final metal definition step.

Experimental Results

Most of the measurements discussed below were performed using the single frequency amplitude modulated remote bias induced electrostatic force microscopy (RB-EFM) setup shown in Fig. 1a. A grounded silicon die is topped with multiple SiO_2 layers with embedded metal electrodes that form an interdigitated structure. The top surface is covered with a grounded aluminum coating that has window openings above this structure. An AC sine-wave bias with a phase difference between the electrodes is applied to them (the classic SIM setup does not include phase difference). The AFM tip is mechanically driven at the first eigenmode free oscillation resonance (RF1, ca. 80 kHz) and is DC-biased, whereas the electrodes AC voltage frequency is chosen at the second eigenmode of the cantilever (RF2, ca. 500 kHz) to decouple the electric and mechanical response. Imaging was performed in dual-pass mode with a lift height of 5 nm to 50 nm during second pass, when the cantilever deflection was demodulated by a lock-in amplifier to yield amplitude, phase, in-phase and quadrature components of oscillation, which are proportional to the electrostatic force acting on the cantilever.

Figure 1b shows a map (bottom) and profile (top) of the in-phase component of the force (in nN) measured over a region with 2-µm deep electrodes. All 8 metal electrodes (lines) are clearly visible as the maxima and minima corresponding to 0° and 180° phase offset, respectively. As will be shown below, the phase offset allows for better resolution of the electrodes.

[1] Certain commercial equipment, instruments, or materials are identified in this paper to adequately specify the experimental procedure. Such identification does not imply recommendation or endorsement by NIST, nor does it imply that the materials or equipment used are necessarily the best available for the purpose.

The graph in Fig. 1b graph overlays an aligned optical image of the imaged region. To demonstrate the usefulness of RB-EFM for subsurface imaging, we decapsulated a commercially available memory IC that has buried metal interconnects and imaged it with SEM and RB-EFM. Figure 1c shows a cross-section of the cleaved IC die with metal interconnects and vias that are buried in an insulator 1.3 µm to 1.8 µm below the surface. A comparison between the SEM and RB-EFM SIM images of two representative regions of the IC die is shown in Fig. 1d. Note that while the SEM secondary electron image is sensitive to the surface topography (i.e. bumps of SiO_2 above the metal lines), RB-EFM images metal lines underneath the surface.

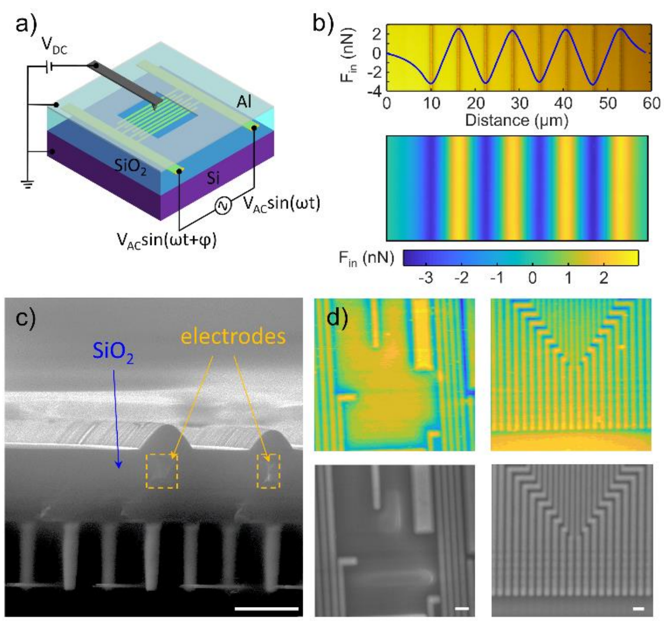

Figure 1. *Experimental setup. a) A Si chip with SiO_2 layers in which metal busses are buried. The two busses are connected to bonding pads forming an interdigitated electrode structure. An AC bias is applied to both busses at the same frequency (RF2) but with a 180° phase shift. A grounded Al coating with a window above the electrode lines is covering the SiO_2 surface. A DC-biased AFM tip is used to image lines by detecting the electrostatic force acting on the cantilever. b) An in-phase force map and profile recorded for 2 µm-deep lines, AC bias of 5 V peak, and a tip DC bias of -6 V. The slant of the image and profile was subtracted for clarity. The graph overlays an optical micrograph of the electrode structure. c) An SEM micrograph of cross-sectioned IC die used for imaging. Metal lines and vias are seen buried ca. 2 µm and 4 µm below the surface. d) RB-EFM in-phase force maps of two regions in the IC die (top row) and corresponding SEM micrographs (bottom row, taken at 30 kV). The scale bars in d)-c) are 2 µm.*

COMSOL Modeling Results

The RB-EFM measurement was simulated using COMSOL MultiPhysics with the electrostatics module. Initially, simulations were done in two-dimensions (2-D), with additional simulations in three-dimensions (3D) to confirm the signal magnitude in the experiment. 2D simulations were scaled into the z-plane (out of the simulation pane) by a function approximating the tip/cantilever profile to get the correct units and signal magnitude, yielding a 2.5D model. Geometry was matched to the test structure of interest and a realistic tip and cantilever shape were used. The simulation used the following model parameters: tip radius (20 nm), leading edge cone angle (20º), trailing edge cone angle (40º), tip length (15 µm), cantilever length (225 µm), cantilever thickness (3 µm), applied AC and DC voltage magnitudes, test structure line width (1.2 µm), and line depth (2 µm). Material parameters were typical values available in the COMSOL library. A typical three-dimensional simulation geometry and resulting potential distribution for RB-EFM are shown in Fig. 2a.

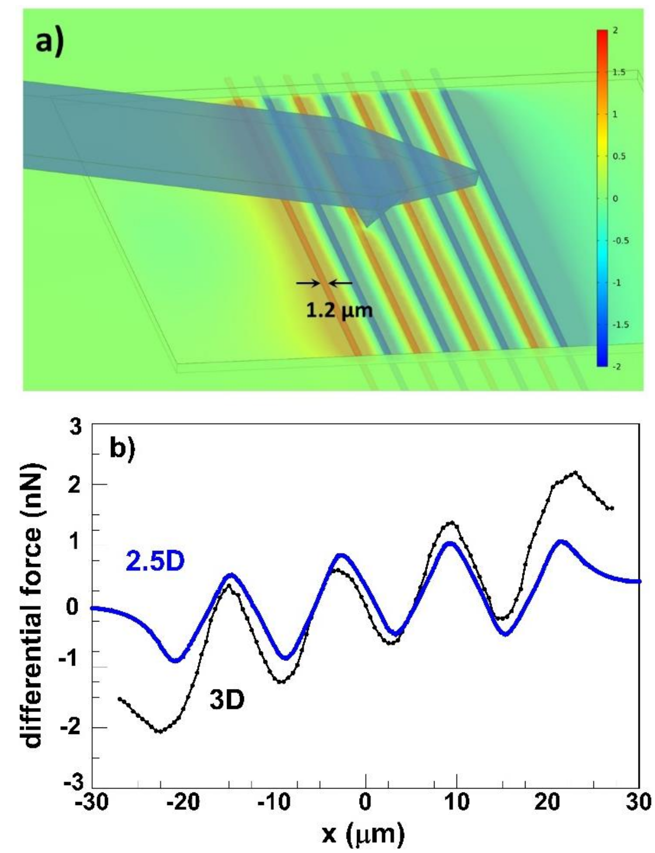

Figure 2. *Simulation results: a) COMSOL geometry of EFM and RB-EFM showing the relevant modeled structures and the simulated potential distribution. The geometry and applied electrical signals are the same as those measured and depicted in Figs. 1a and 1b. b) 2.5D and 3D simulated force on the RB-EFM cantilever, analogous to the measured force shown in Fig. 1b. Note the slant that was subtracted from the experimental data in Fig. 1.*

Electrostatic COMSOL simulations yield potential distributions and the net force between the tip and sample. EFM measures the amplitude (or phase) of the oscillation of a cantilever being driven near a resonance due to an electrostatic force generated by an ac voltage applied to the tip plus any dc potential between the sample and cantilever. To model the EFM cantilever oscillation amplitude from the COMSOL simulation of the tip-sample force, we conducted two simulations, one at the maximum applied excitation voltage and one at the minimum excitation voltage. The tip oscillation amplitude at any point is then easily calculated as the difference between the force at (V_{DC} + ½V_{AC}) and (V_{DC} - ½V_{AC}) scaled by 1/k (the cantilever spring constant.). In this case, V_{AC} is just the magnitude of the applied AC voltage. RB-EFM measures the amplitude (or phase) of the oscillation of a cantilever being driven near a resonance due to an electrostatic force generated by an ac voltage applied to the sample plus any dc potential between the sample and cantilever. In RB-EFM, independent structures can be biased differently. To extract the RB-EFM cantilever oscillation amplitude from the COMSOL simulation of the tip-sample force of two independent sets of buried lines, we used the difference between the force when one set of lines was at (V_{DC} + ½ V_{AC}) and the other at (V_{DC} - ½V_{AC}), and the force with the lines at (V_{DC} - ½ V_{AC}) and the other at (V_{DC} + ½ V_{AC}), also scaled by 1/k. Note that this method produces a static simulation, the results depending on the electrostatically induced cantilever motion being in equilibrium with the applied AC voltage. Cantilever vibrational motion and dynamics are not a factor in the simulation.

Processed simulation results are shown in Fig. 2b. The force on the cantilever is calculated by subtracting the potential differences from two simulations at the opposite extremes of applied voltage. The simulation geometry and parameters were chosen to precisely duplicate the experimental setup in Fig. 1a and the experimental result shown in Fig. 1b. Both 2.5D and 3D simulated differential force agree with the experimentally measured force to within better than a factor of 2. The simulations reproduce the experimental measurements well, tracking the effects of the various applied voltages, line width and depth, and cantilever/tip dimensions. The 2D simulation, when scaled in the z-direction, tracks the full 3D simulation well. Since the scaled 2D simulations are much quicker (less than an hour on a mid-range workstation) compared to a 3D simulation (10's of hours), they are preferred when the structure is strictly 2D or precision agreement is not required. The upward tilt in the simulated signal is due to the interaction of the cantilever with the grounded shield surrounding the test structure. This tilt in the signal is also observed experimentally but has been numerically removed for clarity from the experiment results, in Fig. 1.

Dependence on Imaging Parameters

The critical imaging metrics are the probing depth and lateral resolution, which depend on a range of the experimental parameters: interelectrode phase offset, AC and DC bias amplitudes applied to the electrodes and tip, lift height, and electrode separation distance. Below we discuss these aspects to determine the advantages and limitations of RB-EFM subsurface imaging.

Figure 3 presents profiles of the in-phase, quadrature, and magnitude components of the electrostatic force recorded over 2 µm-deep lines for the phase offset varying from 0° to 180°. At φ = 0°, the magnitude of the force (Fig. 3c, dark red line) rapidly increases when moving from the left towards the first electrode, and then remains high over the whole region containing electrodes. Oscillations, corresponding to individual electrodes are seen on top of this large background force. As φ increases, the background diminishes, until it almost vanishes at φ = 180°, with the individual electrode peaks becoming significantly more prominent (dark blue line, Fig. 3c). The in-phase and quadrature components behave similarly, except for the F_{qd} where the largest peak prominence is seen at φ = 90°. The peak prominence, defined as peak height at maximum relative to the adjacent minima, was calculated for F_{in} and F_{qd} electrode peaks and is plotted in Fig. 3d as a function of φ. Note that the second electrode (from the left) remains as a reference with φ = 0°, whereas φ of the two adjacent electrodes changes, flipping F_{in} on them from negative to positive values (attractive to repulsive force). Interestingly, for these two electrodes, F_{in} peaks disappear at φ = 90° (yellow line, Fig. 3a), but simultaneously reach a maximum in F_{qd} (yellow line Fig. 3b), as expected for in-phase and out-of-phase components. The interelectrode phase dependence implies that the best subsurface imaging conditions are at φ =180 for the force magnitude and F_{in} components. Thus, it is important to not only control the imaging parameters, but also record a specific channel, as resolving power varies between the channels.

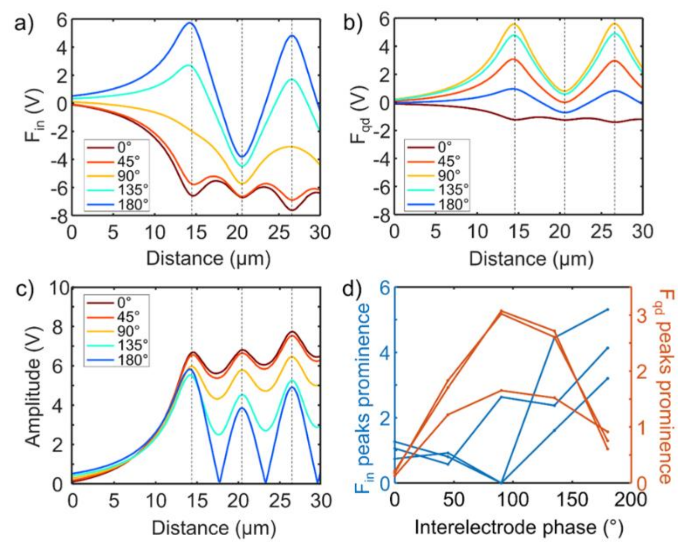

Figure 3. *RB-EFM dependence on the interelectrode phase difference: a) in-phase force, b) quadrature force, and c) force magnitude averaged profiles recorded for 5 V peak AC bias and -6 V tip DC bias on 2 µm-deep lines. The dashed lines indicate the position of metal electrodes. d) Peak prominence for 3 electrodes and both force components as a function of the phase difference between the electrodes. AC bias was applied at RF2; lift height was 5 nm.*

The AC bias dependence of the in-phase force component is shown in Fig. 4a. Here 2 µm deep electrodes were biased as follows: 5 V peak bias was applied to the electrodes indicated with dashed lines and a variable bias from 10 mV to 5 V peak was applied to the electrodes indicated by dash-dotted lines (φ = 180°). F_{in} peak prominence for the electrodes with variable bias is plotted in Fig. 4b, showing a nearly linear voltage dependence. Thus, by selecting the AC voltage magnitude one can not only improve the resolving power of RB-EFM, but also discriminate between different electrodes. Similarly, the application of a DC offset to the buried electrodes in addition to the 5 V peak AC bias changes both the image resolution and allows the discrimination of electrodes (Fig. 4c). Here variation of the DC offset on the electrodes indicated with dash-dotted lines from -2 V to + 2V led to significant changes in contrast and changed the force from repulsive to attractive. The peak prominence of the 3 F_{in} peaks of the electrodes with DC offset has a minimum at ca. -1 V (Fig. 4d) that corresponds to a nearly featureless yellow line in Fig. 4c. At this point ΔV_{ts} in Eq. 2 is close to zero, and CPD is equal to the DC tip bias. A long-range capacitive coupling of the cantilever and tip cone contribute to the detected signal making it non-zero.

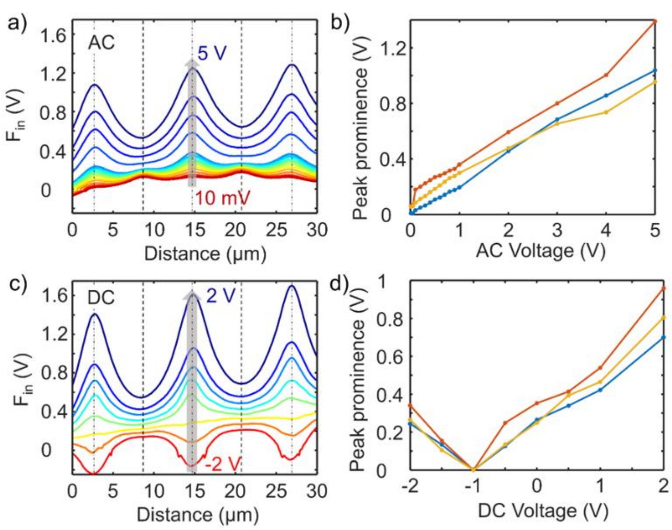

Figure 4. *RB-EFM dependence on the electrode AC and DC voltage bias. a) In-phase electrostatic force component profiles recorded on 2 µm-deep lines with -6 V tip DC bias. Dashed lines indicate electrodes with 5 V peak AC bias, and dash-dotted lines – electrodes with AC bias varying from 10 mV to 5 V peak, as shown by the grey arrow. b) Prominence of 3 peaks in a) corresponding to the AC bias-varying electrodes. c) In-phase electrostatic force component profiles recorded on 2 µm-deep lines with -6 V tip DC bias. Dashed lines indicate electrodes with 5 V peak AC bias, and dash-dotted lines – electrodes with 5 V peak AC bias and a DC offset varying from -2 V to 2 V, as shown by the grey arrow. d) Prominence of 3 peaks in c) corresponding to the DC offset-varying electrodes. Note the minimum at ca. -1 V corresponding to the CPD value. AC bias was applied at RF2; lift height was 5 nm.*

To determine the probing depth of RB-EFM, nine sets of electrodes were measured with buried line depths of 2 µm, 3 µm and 4 µm and interelectrode separations of 6 µm, 8 µm and 10 µm with all other parameters kept the same. In-phase and quadrature component profiles aligned relative to the second electrode peak are shown in Figs. 5a and 5b, respectively. As the depth of the lines increases, the response peaks become shorter and broader, as expected from electric field distribution. The difference between the first and second electrode F_{in} peaks serves as a measure of resolving power and is plotted in Fig. 5c as a function of line depth and for all separation distances. The hand-drawn dashed lines extrapolate dependence beyond the measured range and indicate that the ultimate probing depth at the used experimental parameters is somewhere between 5 µm and 6 µm and is higher for larger separation distances. The lateral resolution metric we chose was the full width at half height of the second (most prominent) F_{in} peak: $FWHM_2$. It was calculated by aligning the F_{in} profiles around zero force and fitting the absolute value of the curve to a gaussian. $FWHM_2$ dependence on the electrode burying depth is shown in Fig. 5d and reflects the significant broadening of the peaks with it. Determining lateral resolution more precisely requires a sample with a single metal electrode, which wasn't available.

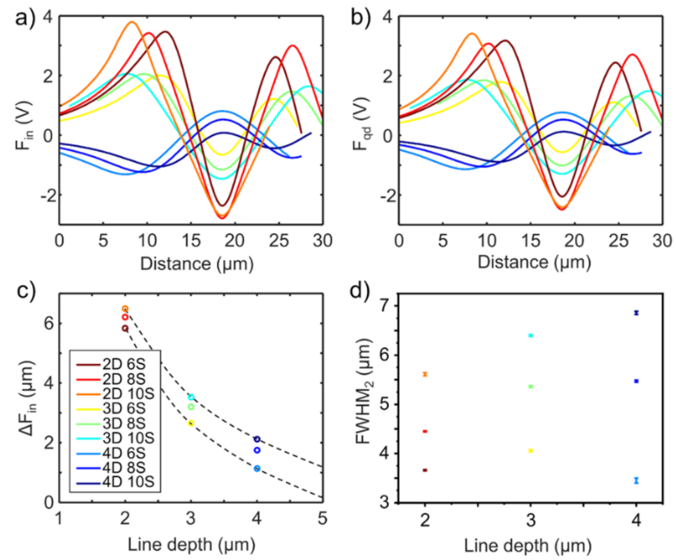

Figure 5. *RB-EFM dependence on the interelectrode separation and burying depth. a) and b) are electrostatic force profile in-phase and quadrature components, respectively measured for the nine test structures with 5 V peak AC bias @RF2 and 180° phase offset to electrodes and -6 V DC tip bias at a lift height of 5 nm. c) Difference between the in-phase force at the first and second electrode peak vs. electrode depth. Dashed lines are for eye guidance. The legend colors are common for all panels and indicate the line depth in micrometers with letter D and interelectrode separation in micrometers with letter S. Thus, the yellow color (3D 6S) stands for the window with electrodes 3 µm deep and 6 µm apart. d) Full width at half maximum of the second electrode peak F_{in} vs. depth. The peaks were fitted to a gaussian after centering them around zero and taking the absolute value, as described in the discussion section.*

Comparison of RB-EFM, EFM and KPFM

It is of interest to compare the RB-EFM results presented here with the imaging capability of classic electric AFM techniques such as EFM and KPFM. Previous reports stated that the maximal probing depth of EFM and KPFM was 1.6 nm and 400 nm, respectively, and of the same order for other AFM techniques (review[13] and refs. therein). The probing depth of the electric AFM techniques depends on the penetration of the electric field through the dielectric and any surface charges.

Therefore, the Debye length of the medium as well as ambient humidity both affect the effective electric field strength above the sample's surface, where it is detected by the cantilever. As we have demonstrated, the application of AC voltage to the buried electrodes and tuning the tip and electrode's DC offset allows for circumventing the screening ability of the dielectric and surface charges and achieve a probing depth in the micrometer range.

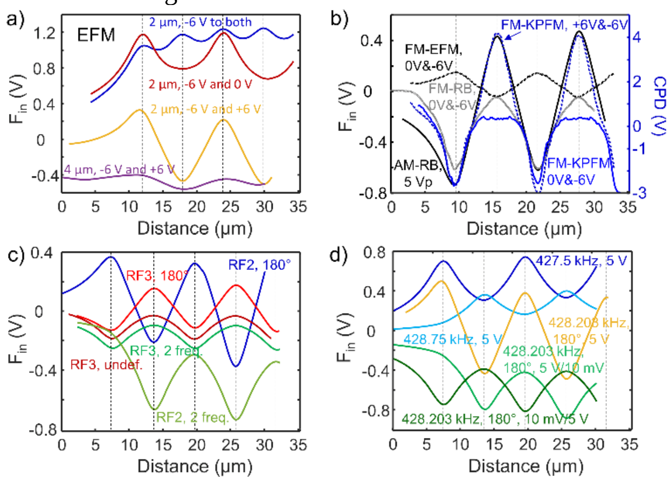

Figure 6. *Comparison of RB-EFM (AM-RB), FM-RB-EFM (FM-RB), EFM and FM-KPFM. a) EFM-measured in-phase electrostatic force profiles recorded on 2 µm and 4 µm-deep lines with 5 V peak tip AC bias and DC electrode bias as indicated in the graph. The dashed lines in all panels indicate electrode positions. b) Electrostatic force in phase component (left y-axis) and CPD (right y-axis) profiles as measured by RB-EFM (5 V peak AC bias to electrodes @ RF2 with 180° phase offset and -6 V DC tip bias), FM-RB-EFM (5 V and 0 V peak AC bias @ 5 kHz to electrodes and 0 V DC tip bias), FM-EFM (-6 V and 0 V DC bias to electrodes and 2 V peak AC tip bias @ 5kHz) and FM-KPFM (-6 V and 0 V/+6V DC bias to electrodes and 2 V peak AC tip bias @ 5kHz) on 2 µm-deep lines. The lift height for all measurements was 35 nm. c) Comparison of single and dual-frequency RB-EFM: phase offset dependence. The shown F_{in} profiles were recorded at indicated eigenmode frequencies and phase shifts of the AC bias applied to the electrodes and 5 nm lift height. 2 µm-deep lines were used. The dual-frequency data (green lines) were recorded simultaneously. d) Comparison of single and dual-frequency RB-EFM: frequency and AC bias dependence. The shown F_{in} profiles were recorded at indicated frequencies and phase shifts of the AC bias applied to the electrodes and 5 nm lift height. 2 µm-deep lines were used. The dual-frequency data (a set of green lines and a set of blue lines) were recorded simultaneously.*

Figure 6a shows F_{in} EFM profiles recorded on the samples discussed above. An AC bias at RF2 was applied to the conductive tip, while a DC bias was applied to the buried electrodes. The blue curve shows a F_{in} distribution for the case of -6 V DC on both sets of 2-µm deep electrodes. Like in the case of RB-EFM with φ = 0°, a strong broad background peak carries a smaller wavy pattern corresponding to electrodes. If one set of electrodes is grounded (red curve, Fig. 6a), the F_{in} curve develops deep troughs, but the background is still high. When electrodes carry + 6V and -6 V, the F_{in} curve (yellow, Fig. 6a) becomes symmetric relative to zero and the background disappears, as the long-range average force on the cantilever vanishes due to the opposite polarity of the electrodes. For the same DC biasing of the 4-µm deep electrodes (purple curve, Fig. 6a), individual peaks are smaller and broader (but still easily detectable) and the whole curve is shifted downwards due to a larger surface charge contribution. Thus, EFM also has a micrometer-range probing depth, and choosing the imaging technique would depend on whether a DC or AC bias can be applied non-destructively to the tested device.

Unlike AM-KPFM, frequency-modulated KPFM has a higher lateral resolution, since frequency shift is proportional not to the first derivative of capacitance, but to the second, which falls off more sharply with distance, thus, limiting the signal contribution mostly to the sharp tip apex. However, subsurface imaging implies a significant spreading of the electric field detected micrometers away from its source, and a better resolution of subsurface structures for the FM mode is not expected. Figure 6b shows a comparison between several different techniques. F_{in} profile recorded with RB-EFM ($V_{B1,2}$ = 5 V peak AC, φ = =180°, V_{tip} = -6 V DC) is shown in black solid curve. Dashed and solid blue curves are CPD profiles measured with FM-KPFM (0.75 V @ 5 kHz, sideband detection) for V_{B1} = + 6 V, V_{B2} = - 6 V and V_{B1} = 0 V, V_{B2} = - 6 V, respectively. Although the FM-KPFM resolves better the surface charge distribution, which can be seen in the bumpy flat tops of the solid blue curve for the grounded electrodes, the biased electrodes CPD peaks are no sharper than the F_{in} RB-EFM peaks. Similarly, the FM-RB-EFM F_{in} grey curve has only slightly sharper electrode peaks but falls off to zero faster outside the electrode area on the left than the RB-EFM black solid curve. Finally, the F_{in} dashed black curve measured by FM-EFM also has a higher surface lateral resolution but not a significant improvement in resolving the subsurface electrodes. Note that FM modes are significantly slower than the AM ones, since the phase-locked-loop required to detect frequency shift limits the measurement bandwidth.

Distinguishing between different interconnects in an IC die can be done by varying AC and DC voltage magnitudes, as shown above. A faster way could be simultaneous signal detection at multiple frequencies corresponding to AC excitations applied to different pins. However, RB-EFM relies on the free oscillation eigenmodes to boost the sensitivity. Higher eigenmodes have much smaller resonance peaks than the principle one, and only a few are practically usable. Since RF1 (≈ 70 kHz) is used for topography detection, RF2 (≈ 400 kHz) and RF3 (≈ 1.2 MHz) can be employed for double-frequency (DF) detection. Figure 6c compares SF RB-EFM F_{in} profiles recorded at RF2 (blue curve) and RF3 (light red curve) with φ = 180°. At RF3 the signal is weaker but still very strong. When φ is set to an undefined state by increasing the frequency of one bus by several Hz above RF3, and keeping the other at RF3, the resolution drops down (dark red curve, Fig. 6c), but both electrodes' peaks are still visible (cf. light and dark red curves, Fig. 6c). Finally, when DF RB-EFM is used by exciting one bus at RF2 and the other at RF3 with the same amplitude, and demodulating both channels, the two electrodes can be easily discerned. The first electrode from the left (Fig. 6c) has a clear peak at RF3 (dark green curve), but none at RF2 (light green curve). Minima in both curves correspond to the electrodes biased at the respective frequencies. DF detection does not require using two separate eigenmodes. Two frequencies can be selected slightly below and above the RF. Figure 6d compares SF RB-EFM F_{in} yellow curve detected at RF2 and two DF RB-EFM F_{in} blue curves detected at RF2+0.547 kHz and RF2-0.703 kHz. While the latter two have a slightly lower magnitude (relative to the background), their maxima clearly correspond to the electrodes biased at corresponding frequencies, as the minima in the case of Fig. 6c green curves. Figure 6c also compares DF detection with SF detection at different AC magnitudes: light and dark green curves were recorded at RF2 with V_{B1} = 5 V, V_{B2} = 10 mV and V_{B1} = 10 mV and V_{B2} = 5 V. Here the curves' minima correspond to the electrodes biased at 5 V.

Conclusions

We have demonstrated a new variation of electrostatic force microscopy, remote bias induced EFM, where the electrostatic force vibration is induced by a bias applied to remote structures. By controlling the phase of the AC signal applied to distinct structures we can improve differentiation between them in the resulting image of cantilever amplitude or phase. A COMSOL Multiphysics model has been developed that precisely models the measured RB-EFM, EFM, and KPFM images of the test structures, reproducing all essential features and predicting response. Experimental and modeling results confirm that we can resolve geometries useful for integrated circuits to depths of up to 6 micrometers (in SiO_2). We compared RB-EFM, conventional EFM and KPFM, determining the limitations and advantages of each technique. We showed that by biasing independent line traces at frequencies that were small deltas from a cantilever resonance frequency, we could still differentiate these different line traces with RB-EFM. This later capability could prove useful for failure analysis and fault location in real integrated circuit back end of the line processes.

Acknowledgments

This work was partially supported by the NIST/Georgetown PREP Program (70NANB18H161). Contribution of the National Institute of Standards and Technology, not subject to copyright in the United States of America.

References

[1] K.T. Chung, J H. Reisner, and E.R. Campbell, "Charging Phenomena in the Scanning Electron Microscopy of Conductor-Insulator Composites: A Tool for Composite Structural Analysis," *J. Appl. Phys.*, Vol. 54 (1983), p 6099-6112. doi: 10.1063/1.331946

[2] S.P. Frigo, Z.H. Levine, N.J. Zaluzec, "Submicron Imaging of Buried Integrated Circuit Structures Using Scanning Confocal Electron Microscopy," *Appl. Phys. Lett.*, Vol. 81, (2002), p 2112-2114. doi: 10.1063/1.1506010

[3] J.Z. Kovacsa, K. Andresena, J.R. Paulsa, C. Pardo Garciaa, M. Schossigb, K. Schultec, W. Bauhofera, "Analyzing the Quality of Carbon Nanotube Dispersions in Polymers Using Scanning Electron Microscopy. *Carbon," Vol. 45, (2007), p 1279-1288.* doi: 10.1016/j.carbon.2007.01.012

[4] E. C. Cosgriff, A. J. D'Alfonso, L. J. Allen, S. D. Findlay, A. I. Kirkland, P. D. Nellist, "Three-Dimensional Imaging in Double Aberration-Corrected Scanning Confocal Electron Microscopy Part I: Elastic Scattering," *Ultramicroscopy*, Vol. 108 (2008), p 1558-1566. doi: 10.1016/j.ultramic.2008.05.009

[5] S. Bals, S. Van Aert, J. Verbeeck, D. Van Dyck, "Advanced Electron Microscopy for Advanced Materials," *Adv. Mater.*, Vol. 24 (2012), p 5655-5675. doi: /10.1002/adma.201202107

[6] Z. Minhua, M. Bin, K. Jae-Woo, J. G. Luke, G. Xiaohong, N. Tinh, P. Cheol, T. L. Peter, J. S. Villarrubia, E. V. András, J. A. Liddle, "New Insights into Subsurface Imaging of Carbon Nanotubes in Polymer Composites via Scanning Electron Microscopy," *Nanotechnology*, Vol 26 (2015), p 085703. doi: 10.1088/0957-4484/26/8/085703

[7] A. O. Oladipo, A. Lucibello, M. Kasper, S. Lavdas, G. M. Sardi, E. Proietti, F. Kienberger, R. Marcelli, N. C. Panoiu, "Analysis of a Transmission Mode Scanning Microwave Microscope for Subsurface Imaging at the Nanoscale," *Applied Physics Letters*, Vol. 105, (2014), p 133112. doi: 10.1063/1.4897278.

[8] J. J. Kopanski, L. You, J.-J. Ahn, E. Hitz, Y. S. Obeng, "Scanning Probe Microscopes for Subsurface Imaging," *ECS Transactions*, Vol. 61 (2014), p 185-193. doi: 10.1149/06102.0185ecst

[9] J. D. Chisum, Z. Popovic, "Performance Limitations and Measurement Analysis of a near-Field Microwave Microscope for Nondestructive and Subsurface Detection," *IEEE Trans. Microwave Theory and Techniques*, Vol. 60 (2012), p 2605-2615. doi: 10.1109/TMTT.2012.2201739

[10] K. Haddadi, D. Glay, T. A. Lasri, "A 60 GHz Scanning near-Field Microscope with High Spatial Resolution Sub-Surface Imaging," *IEEE Microwave and Wireless Components Letters*, Vol. 21 (2011) p 625-627. doi: 10.1109/lmwc.2011.2167744

[11] M. Zhao, X. Gu, S. E. Lowther, C. Park, Y. C. Jean, T. Nguyen, "Subsurface Characterization of Carbon Nanotubes in Polymer Composites via Quantitative Electric Force Microscopy," *Nanotechnology*, Vol. 21, (2010), p 225702. doi: 10.1088/0957-4484/21/22/225702

[12] A. C. Diebold, "Subsurface Imaging with Scanning Ultrasound Holography," *Science*, Vol. 310 (2005), *p* 61-62. doi: 10.1126/science.1119259]

[13] M. Soliman, Y. Ding, L. Tetard, "Nanoscale Subsurface Imaging," *J. Physics: Condensed Matter*, Vol. 29 (2017), p 173001. doi: 10.1088/1361-648X/aa5b4a

[14] P. T. Lillehei1, J.-W. Kim, L. J. Gibbons, C. Park, "Quantitative Assessment of Carbon Nanotube Dispersion in Polymer Matrices," *Nanotechnology*, Vol.

20 No. 32 (2009), p 325708. doi: 10.1088/0957-4484/20/32/325708
[15)] W, Li, S. T. Buschhorn, K. Schulte, W. Bauhofer, "The Imaging Mechanism, Imaging Depth, and Parameters Influencing the Visibility of Carbon Nanotubes in a Polymer Matrix Using an SEM," *Carbon*, Vol, 49, (2011) p 1955-1964. doi: 10.1016/j.carbon.2010.12.069
[16] O. Jbara, S. Fakhfakh, M. Belhaj, S. Rondot, "Charge Implantation Measurement on Electron-Irradiated Insulating Materials by Means of a SEM Technique," *Microsc. Microanal.*, Vol. 10, No. 6 (2004), p 697-710. DOI: 10.1017/s1431927604040644
[17] H. Guo, A. Yulaev, E. Strelcov, A. Tselev, C. Arble, A.E. Vladar, J.S. Villarrubia, A. Kolmakov, "Probing Electrified Liquid–Solid Interfaces with Scanning Electron Microscopy," *ACS Appl. Mater. Interfaces*, Vol. 12, No. 50 (2020), p 56650–56657 doi.org: 10.1021/acsami.0c19634
[18] A. Orozco, "Magnetic Field Imaging for Electrical Fault Isolation," in *Microelectronics Failure Analysis: Desk Reference (Seventh Edition)*, T. Ganghi, Ed., ASM International (Materials Park, OH, USA, 2019), p 111-131. doi: 10.31399/asm.tb.mfadr7.t91110111
[19] J. Gaudestad, A. Orozco, "Magnetic Field Imaging for Non-Destructive 3D IC Testing," *Microelectronics Reliability*, Vol. 54 (2014), p 2093-2098. doi: 10.1016/j.microrel.2014.07.080
[20] D. Vallett, J. Gaudestad, C. Richardson, "High-Resolution Backside GMR Magnetic Current Imaging on a Contour-Milled Globally Ultrathin Die," in *ISTFA 2014: Conference Proceedings from the 40th International Symposium for Testing and Failure Analysis*, ASM International: 2014; pp 23-27. doi: 10.31399/asm.cp.istfa2014p0023
[21] H. Yamada, "AFM Measurement in Liquid," in *Roadmap of Scanning Probe Microscopy*, Morita, S., Ed. Springer Berlin Heidelberg: (Berlin, Heidelberg, 2007); p 101-108. doi: 10.1007/978-3-540-34315-8_13
[22] L. You, J-J. Ahn, Y.S. Obeng, J.J. Kopanski, "Subsurface Imaging of Metal Lines Embedded in a Dielectric with a Scanning Microwave Microscope," *J. Physics D: Applied Physics*, Vol. 49, No. 4, (2016), p 045502. doi: 10.1088/0022-3727/49/4/045502
[23] M. Emmrich, F. Huber, F. Pielmeier, J. Welker, T. Hofmann, M. Schneiderbauer, D. Meuer, S. Polesya, S. Mankovsky, D. Ködderitzsch, H. Ebert, F.J. Giessibl, "Subatomic Resolution Force Microscopy Reveals Internal Structure and Adsorption Sites of Small Iron Clusters," *Science*, Vol. 348 (2015), p 308-311. doi: 10.1126/science.aaa5329
[24] S.V. Kalinin, D.A. Bonnell, "Scanning Impedance Microscopy of Electroactive Interfaces," *Appl. Phys. Lett.*, Vol. 78, No. 9, (2001), p 1306-1308. doi: 10.1063/1.1350627
[25] S.V. Kalinin, D.A. Bonnell, "Scanning Impedance Microscopy of an Active Schottky Barrier Diode," *J. Appl. Phys.*, Vol. 91, No. 2 (2002), p 832-839. doi: 10.1063/1.1427145
[26] L. Fumagalli, M.A. Edwards, G. Gomila, "Quantitative Electrostatic Force Microscopy with Sharp Silicon Tips," *Nanotechnology*, Vol. 25, No. 49 (2014), p 495701. doi: 10.1088/0957-4484/25/49/495701
[27] S. Yongho, J. Wonho, "Atomic Force Microscopy and Spectroscopy," *Reports on Progress in Physics*, Vol. 71, No. 1, (2008), p 016101. doi: 10.1088/0034-4885/71/1/016101
[28] C.H. Lei, A. Das, M. Elliott, J.E. Macdonald, "Quantitative Electrostatic Force Microscopy-Phase Measurements," *Nanotechnology*, Vol 15, No. 5 (2004), p 627-634. doi: 10.1088/0957-4484/15/5/038
[29] A. Gil, J. Colchero, J. Gómez-Herrero, A.M. Baró, "Electrostatic Force Gradient Signal: Resolution Enhancement in Electrostatic Force Microscopy and Improved Kelvin Probe Microscopy," *Nanotechnology*, Vol. 14, No. 2 (2003), p 332-340. doi: 10.1088/0957-4484/14/2/345
[30] G. Paul, "Electrostatic Force Microscopy: Principles and Some Applications to Semiconductors," *Nanotechnology, Vol. 12. No. 4 (2001)*, p 485-490. doi: 10.1088/0957-4484/12/4/321
[31] W. Melitz, J. Shen, A.C. Kummel, S. Lee, "Kelvin Probe Force Microscopy and Its Application," *Surf. Sci. Rep.*, Vol 66 (2011), p 1-27. doi: 10.1016/j.surfrep.2010.10.001
[32] S.V. Kalinin, S. Jesse, J. Shin, A.P. Baddorf, M.A. Guillorn, D.B. Geohegan, "Scanning Probe Microscopy Imaging of Frequency Dependent Electrical Transport through Carbon Nanotube Networks in Polymers," *Nanotechnology*, Vol. 15, No. 8 (2004), p 907-912. doi: 10.1088/0957-4484/15/8/006
[33] T.S. Jespersenaand, J. Nygård, "Mapping of Individual Carbon Nanotubes in Polymer/Nanotube Composites Using Electrostatic Force Microscopy," *Appl. Phys. Lett.*, Vol. 90 (2007), p 183108. doi: 10.1063/1.2734920
[34] M.J. Cadena, R. Misiego, K.C. Smith, A. Avila, B. Pipes, R. Reifenberger, A. Raman, "Sub-Surface Imaging of Carbon Nanotube–Polymer Composites Using Dynamic AFM Methods," *Nanotechnology*, Vol. 24, No. 13 (2013) p 135706. doi:10.1088/0957-4484/24/13/135706
[35] S. Patel, C.W. Petty, K. Krafcik, B. Loyola, G. O'Bryan, R.W. Friddle, "Imaging Latex–Carbon Nanotube Composites by Subsurface Electrostatic Force Microscopy," *Nanotechnology*, Vol. 27. No. 41 (2016), p 415705. doi: 10.1088/0957-4484/27/41/415705
[36] L. You, J.-J. Ahn, E. Hitz, J. Michelson, Y.S. Obeng, J.J. Kopanski, "Electromagnetic Field Test Structure Chip for Back End of the Line Metrology," Proc. *2015 International Conference on Microelectronic Test Structures (ICMTS 2015)*, Tempe, AZ, March 2015, p 235-239. doi: 10.1109/ICMTS.2015.7106101